Industrial Chemistry & Materials

ROYAL SOCIETY OF CHEMISTRY

PAPER

View Article Online
View Journal

Check for updates

Cite this: DOI: 10.1039/d6im00028b

Site-specific atomic ordering in Pt-based high-entropy alloys for enhanced methanol oxidation

Guangtao Mao,[a] Xiyue Han,[a] Yuan Xiong,[a] Leqing Luo,[a] Zhouxun Zeng[a] and Qingmei Wang *[abc]

High-entropy alloys (HEAs) have emerged as promising electrocatalysts due to their unique structural and electronic properties. In this study, we report the synthesis of a class of site-specific atomic ordering high-entropy alloy nanoparticles supported on hollow mesoporous carbon spheres (Pt-HEA-*x*/HMCSs), whereby a silica-confined synthesis strategy guided by precise thermal field engineering promotes site-specific substitution and the emergence of a chemically ordered phase. The special-aberration-corrected high-angle annular dark-field scanning transmission electron microscopy (AC-HAADF-STEM) characterization revealed that Pt-HEA-6/HMCSs (PtFeNiCuCoRu/HMCSs) possess an ordered atomic structure with compressive lattice strain. The typical sample (Pt-HEA-6/HMCSs) displays pronounced lattice compression and an optimized coordination environment, as evidenced by X-ray absorption fine structure (XAFS) results. This is directly demonstrated by the contraction of the Pt–M (M: Cu, Ni, Ru, Co, Fe, and Pt) bond length to 2.31 Å from 2.53 Å in pristine Pt foil and a modified coordination environment (Pt–Pt coordination number: 11.24 *vs.* 12), which collectively lead to the modulation of its electronic structure. In addition, ultraviolet photoemission spectroscopy (UPS) and X-ray photoelectron spectroscopy (XPS) analyses revealed the modulation of the electronic structure, which optimized the Pt d-band center, and a consequent enhancement of the electrocatalytic activity. The aforementioned characteristics collectively contribute to enhanced electrocatalytic performance. Specifically, the Pt-HEA-6/HMCS catalyst demonstrates a mass activity (MA) of 1.54 mA μg_{Pt}^{-1} and a specific activity (SA) of 1.07 mA cm^{-2}, which are 6.42 and 3.45 times that of the commercial Pt/C benchmark, respectively. At a fixed potential of 1.0 V *vs.* RHE, Pt-HEA-6/HMCSs also exhibit the highest MA and SA among all catalysts. Furthermore, they exhibit improved CO tolerance, demonstrated by a 206 mV negative shift in the CO oxidation onset potential compared with Pt/C and the complete oxidation of adsorbed CO at 0.5 V as revealed by *in situ* Fourier transform infrared-diffuse reflection (FTIR), alongside enhanced stability with only 12.7% current density loss after accelerated durability testing. The enhanced performance is attributed to the synergistic effects of chemical ordering, lattice strain and strong metal–metal interactions. This work provides a feasible pathway for designing highly efficient and stable HEA-based electrocatalysts for fuel cell applications.

Keywords: Methanol oxidation reaction; Site-specific substitution; Atomic ordering; Electronic modulation; High-entropy alloys.

Received 21st January 2026,
Accepted 26th March 2026

DOI: 10.1039/d6im00028b

rsc.li/icm

Open Access Article. Published on 31 March 2026. Downloaded on 5/11/2026 10:52:48 PM.
This article is licensed under a Creative Commons Attribution-NonCommercial 3.0 Unported Licence.

1 Introduction

Direct methanol fuel cells (DMFCs) have attracted considerable attention as clean energy conversion devices owing to their superior energy density and environmental friendliness.[1–8] However, the widespread commercialization of DMFCs is hindered by the sluggish kinetics of the anode alcohol oxidation reactions and the severe poisoning of Pt-based catalysts by CO-like intermediates.[9–20] Although significant efforts have been devoted to developing Pt-based alloy catalysts to improve catalytic activity and anti-poisoning ability, conventional binary or ternary alloys still suffer from limited active sites, poor stability, and insufficient tunability of electronic structures.[21–28]

Recently, high-entropy alloys (HEAs) have opened new avenues for designing advanced electrocatalysts.[29–35] The unique cocktail effect, lattice distortion, and high-entropy stabilization endow HEAs with tunable electronic structures and exceptional catalytic properties.[36] Moreover, the

[a] *School of Chemistry and Chemical Engineering, Guizhou University, Guiyang, Guizhou, 550025, China. E-mail: qmwang3@gzu.edu.cn*
[b] *Guizhou Provincial Key Laboratory of Green Chemical and Clean Energy Technology, Guiyang, Guizhou, 550025, China*
[c] *Guizhou Provincial Key Laboratory of Green Catalysis and Materials for Resource Conversion, Guiyang, Guizhou, 550025, China*

© 2026 The Author(s). Co-published by the Institute of Process Engineering, Chinese Academy of Sciences and Royal Society of Chemistry

Open Access Article. Published on 31 March 2026. Downloaded on 5/11/2026 10:52:48 PM. This article is licensed under a Creative Commons Attribution-NonCommercial 3.0 Unported Licence.

incorporation of multiple transition metals can modulate the d-band center of Pt, thereby weakening the adsorption of poisonous species and enhancing the oxidation efficiency.[37] However, the vast majority of reported HEA electrocatalysts are random solid solutions, synthesized under harsh conditions (*e.g.*, rapid high-temperature pyrolysis) that promote elemental mixing but lack atomic-level control.[38] This often results in a disordered atomic arrangement, which fails to fully exploit the potential for optimizing specific active sites and falls short of achieving the theoretically predicted synergistic effects.[39] Furthermore, the ubiquitous challenges of nanoparticle agglomeration and weak metal–support interaction further impede their practical application.[40] Consequently, the precise synthesis of site-selective atomic ordering HEA nanoparticles with uniform dispersion and robust metal–support interaction remains a formidable challenge.

Herein, we developed a silica-confined, thermally regulated synthesis strategy to address these limitations. By employing precise control over the heating rate, annealing temperature, and dwelling time, we circumvent the formation of disordered solid solutions. This meticulous thermal field engineering promotes site-specific substitution and preferential nucleation, guiding the formation of a unique class of Pt-based HEA nanoparticles with a chemically ordered intermetallic structure, which are firmly anchored on hollow mesoporous carbon spheres (HMCSs). The resulting catalyst thus possesses a chemically ordered atomic arrangement, compressive lattice strain, and optimized electronic structure, which collectively contribute to enhance electrocatalytic performance for both methanol and ethanol oxidation reactions. This orderly arrangement is mainly due to the fact that various transition metal atoms occupy specific lattice positions of Pt, and alternate with Pt. The claim of "site-specific atomic ordering" refers to the precise arrangement where different atoms occupy designated crystallographic positions rather than random mixing. Special-aberration-corrected high-angle annular dark-field scanning transmission electron microscopy (AC-HAADF-STEM) provides direct evidence for the site-specific atomic ordered structure in Pt-HEA-6/HMCSs. Simultaneously, Pt-HEA-6/HMCSs display characteristic lattice compression, with measured interplanar spacings of d_{111} = 0.213 and d_{110} = 0.269 nm. X-ray absorption fine structure (XAFS) analysis reveals the presence of under-coordinated Pt sites in Pt-HEA-6/HMCSs (coordination number: 11.24) and a contracted Pt–M bond length of 2.31 Å, compared to 2.53 Å in Pt foil, collectively indicating effective electronic structure modulation and lattice strain. In addition, ultraviolet photoemission spectroscopy (UPS) and X-ray photoelectron spectroscopy (XPS) analyses revealed the modulation of the electronic structure, which optimized the Pt d-band center, and a consequent enhancement of the electrocatalytic activity. Specifically, the Pt-HEA-6/HMCS catalyst demonstrates a mass activity (MA) of 1.54 mA μg_{Pt}^{-1} and a specific activity (SA) of 1.07 mA cm^{-2}, which are 6.42 and 3.45 times that of the commercial Pt/C benchmark, respectively. Furthermore, they exhibit improved CO tolerance, demonstrated by a 206 mV negative shift in the CO oxidation onset potential compared with Pt/C and the complete oxidation of adsorbed CO at 0.5 V as revealed by *in situ* Fourier transform infrared-diffuse reflection (FTIR), alongside enhanced stability with only 12.7% current density loss after accelerated durability testing. Through a combination of structural characterization and electrochemical analysis, we elucidate the roles of chemical ordering, lattice strain, and multi-element synergy in enhancing the catalytic activity and stability. This study not only presents a highly efficient HEA electrocatalyst but also offers deep insights into the design principle of multi-metallic catalysts for energy conversion technologies.

2 Results and discussion

2.1 Microstructural and crystallographic analysis

Fig. 1a shows the synthesis process of ordered HEA/HMCS NPs. Firstly, SiO_2@SiO_2/RF nanospheres with a core–shell structure were synthesized for use as a hard template following a literature method.[41–43] The prepared SiO_2@SiO_2/RF nanospheres are uniformly distributed and of uniform size (Fig. S1). Following this, precise thermal annealing under a controlled atmosphere facilitated the co-reduction and carbonization steps, after which a selective etching process removed the silica framework to reveal the well-defined hollow carbon spheres supporting the HEA nanoparticles (HEA/HMCSs). The positive shift in the X-ray diffraction (XRD) diffraction peaks to higher 2θ angles for the as-prepared samples, relative to Pt/C (Fig. 1b–d), confirms their single-phase solid solution nature.[44] Meanwhile, we load Pt single metal onto HMCSs for comparison (Fig. S2). The presence of the (110) superlattice diffraction peak at 2θ = 33.27° in the samples, coupled with its consistency with standard FePt/CoPt patterns (PDF#43-1359, PDF#43-1358), suggests the establishment of a face-centered tetragonal phase. The intensity ratio of the (110) to (111) reflections was employed to quantify the ordering degree in the HEA catalysts.[45] Lattice parameters and the order degree determined from XRD data are listed in Table S1. Interestingly, with the introduction of the Co atom, the degrees of ordering of Pt-HEA-6/HMCSs (0.43) and HEA-5/HMCSs (0.41) are significantly higher than that of Pt- and Pt-HEA-4/HMCSs (0.33). Simultaneously, the lattice strain observed for Pt-HEA-*x*/HMCSs, calculated from the Pt(111) Bragg reflection, increases sequentially (2.81% for Pt-HEA-4/HMCSs, 3.26% for Pt-HEA-5/HMCSs, and 4.44% for Pt-HEA-6/HMCSs; Table S1). This synergistic enhancement suggests that integrating multi-level co-catalytic components is an effective strategy for concurrently optimizing the site-specific atomic ordered structure and enhancing the lattice strain.

A suite of characterization techniques was employed to probe the microstructural features and atomic configurations of the samples, including transmission electron microscopy (TEM), scanning electron microscopy (SEM), AC-HAADF-STEM, energy-dispersive X-ray spectroscopy (EDX), and energy-loss spectroscopy (EELS). After further high-temperature co-reduction carbonization treatment and acid etching, the

© 2026 The Author(s). Co-published by the Institute of Process Engineering, Chinese Academy of Sciences and Royal Society of Chemistry

Open Access Article. Published on 31 March 2026. Downloaded on 5/11/2026 10:52:48 PM.
This article is licensed under a Creative Commons Attribution-NonCommercial 3.0 Unported Licence.

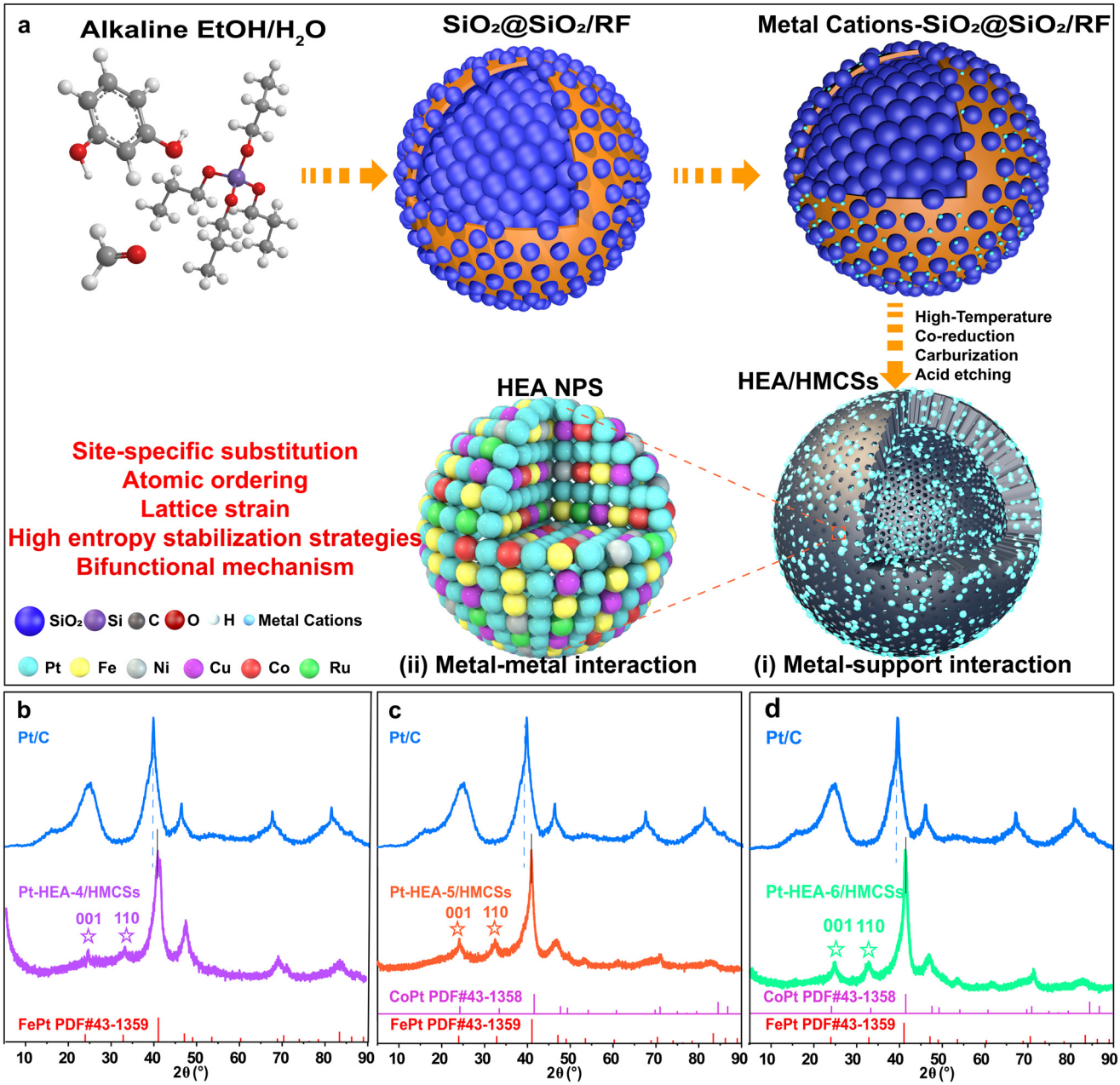

Fig. 1 (a) Schematic of ordered HEA/HMCS NP synthesis; XRD pattern of the as-synthesized (b) Pt-HEA-4/HMCSs, (c) Pt-HEA-5/HMCSs and (d) Pt-HEA-6/HMCSs.

obtained sample particles are evenly distributed, and the partially collapsed particles initially indicate a hollow structure within (Fig. S3). Fig. 2a further demonstrates the hollow structure and surface porous structure of the sample. Fig. 2b shows that HEA NPs are uniformly distributed in the form of nanoparticles on the surface of HMCSs, with an average particle size of 2.92 nm (Fig. S3a). This diminution in particle size thus enhances the accessibility of atomic-scale reaction centers, thereby maximizing the utilization of the enlarged specific surface area.[46] At the same time, which means that after annealing treatment, SiO_2 shells can successfully avoid agglomeration and sintering of HEA NPs. AC-HAADF-STEM imaging and the corresponding Fourier transform (FFT) analysis (Fig. 2c inset) reveal a site-specific atomic order arrangement within the Pt-HEA-6/HMCSs, confirming a crystalline phase. The measured (111) and (110) lattice spacings of 0.213 nm and 0.269 nm for Pt-HEA-6/HMCSs indicate the presence of compressive stress, attributed to atomic mismatch from multielemental doping. Furthermore, the homogeneous distribution of all elements, as confirmed by EDS mapping (Fig. 2d_1–d_7) and the absence of segregation in EELS line scans (Fig. 2e), verifies the atomic-scale mixing and high-entropy nature of the NPs.[47] In addition, the HMCSs exhibit a core diameter of 314 nm and an average shell width of

© 2026 The Author(s). Co-published by the Institute of Process Engineering, Chinese Academy of Sciences and Royal Society of Chemistry

Open Access Article. Published on 31 March 2026. Downloaded on 5/11/2026 10:52:48 PM.
This article is licensed under a Creative Commons Attribution-NonCommercial 3.0 Unported Licence.

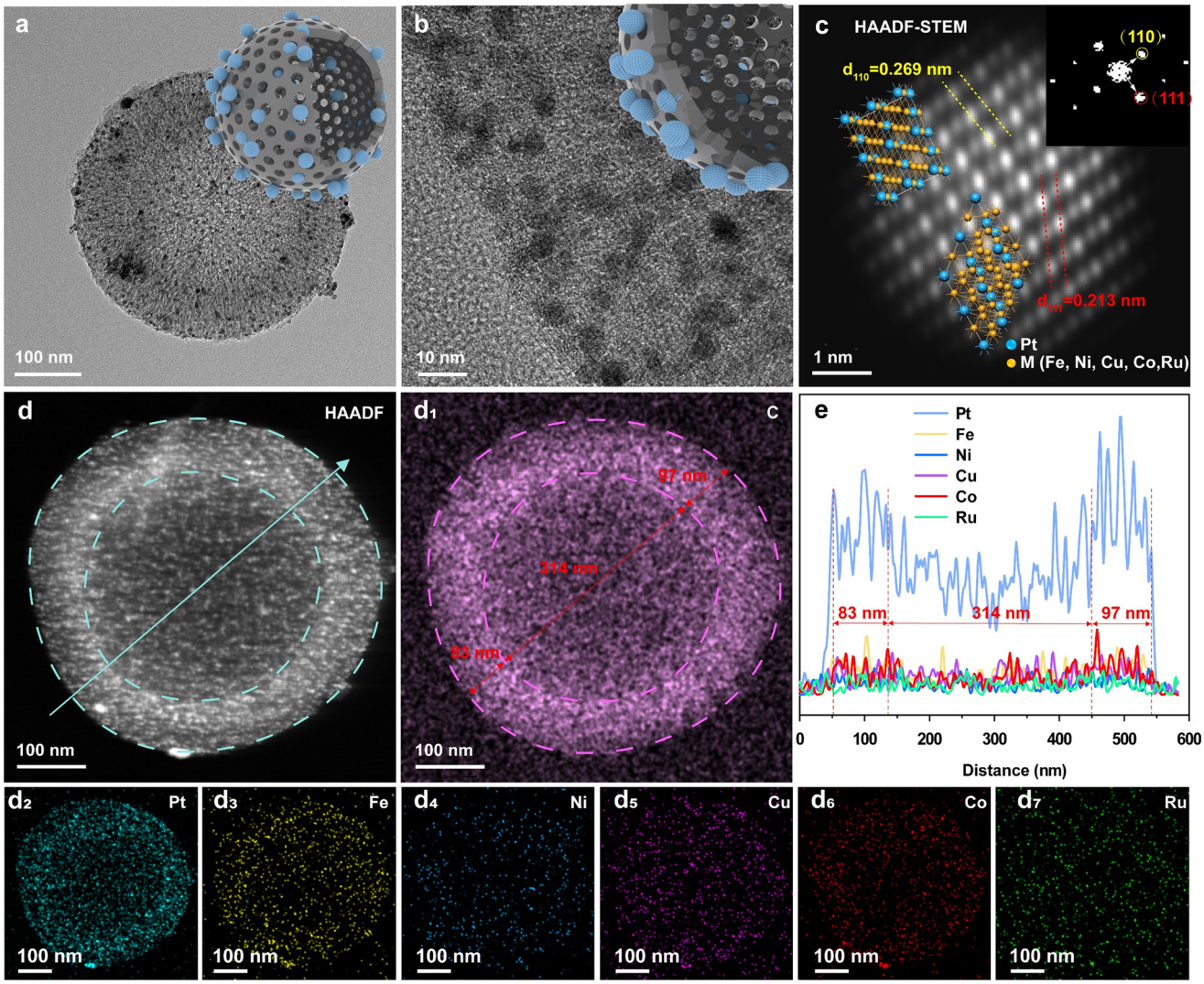

Fig. 2 Pt-HEA-6/HMCS catalyst characterized by (a and b) TEM and (c) AC-HRTEM-STEM (inset is the corresponding Fourier transform diffraction pattern); (d and d_1–d_7) composition of Pt-HEA-6/HMCSs probed by EDX elemental mapping and (e) associated EELS data.

approximately 90 nm. Coupled with the surface porous structure, this morphology provides a large surface area, thereby exposing more active sites during the reaction. In addition, detailed characterization of the HMCSs' porous structure was performed *via* N_2 adsorption–desorption measurements (BSD-PM2 analyzer). The Brunauer–Emmett–Teller (BET) method and Barrett–Joyner–Halenda (BJH) model were employed to determine the specific surface area and pore size distribution, respectively. As shown in Fig. S5a, the recorded isotherm was a type IV isotherm with an H3-type hysteresis loop, which might be caused by the surface hierarchical porous structure.[48] Meanwhile, a specific surface area of 1185.3 $m^2\ g^{-1}$ provides more site attachment points for high-entropy alloy nanoparticles to accelerate the kinetics of electrocatalytic reactions. The pore size distribution map indicates that there are mesoporous structures of about 2 nm and 5–9 nm on their surface, further verifying their hierarchical porous structure (Fig. S5b).

XAFS analysis delineated the atomic coordination and electronic configuration in Pt-HEA-6/HMCSs. The Pt L_3-edge X-ray absorption near-edge structure (XANES) spectrum (Fig. 3a) indicated a metallic state for Pt, with an absorption peak intensity at the L_3-edge comparable to that of Pt foil, suggesting a near-metallic state with a modified electronic structure. Extended X-ray absorption fine structure (EXAFS) analysis (Fig. 3b) showed a primary coordination peak at ~2.31 Å, attributed to Pt–Pt/Pt–M bonds, which is notably shorter than that in Pt foil (2.53 Å), indicating significant lattice compressive strain, consistent with XRD results (Table S1). EXAFS fitting (Fig. 3c and S6) and wavelet transform (WT) analysis (Fig. 3f_1–f_3) further confirmed the distinct local coordination environment of Pt. Quantitative analysis yielded a Pt coordination number of 11.24, lower than the value of 12 for bulk Pt (Table S2). The above-mentioned experiment confirms the presence of compressive lattice strain and an optimized coordination environment in the synthesized

© 2026 The Author(s). Co-published by the Institute of Process Engineering, Chinese Academy of Sciences and Royal Society of Chemistry

Open Access Article. Published on 31 March 2026. Downloaded on 5/11/2026 10:52:48 PM.
This article is licensed under a Creative Commons Attribution-NonCommercial 3.0 Unported Licence.

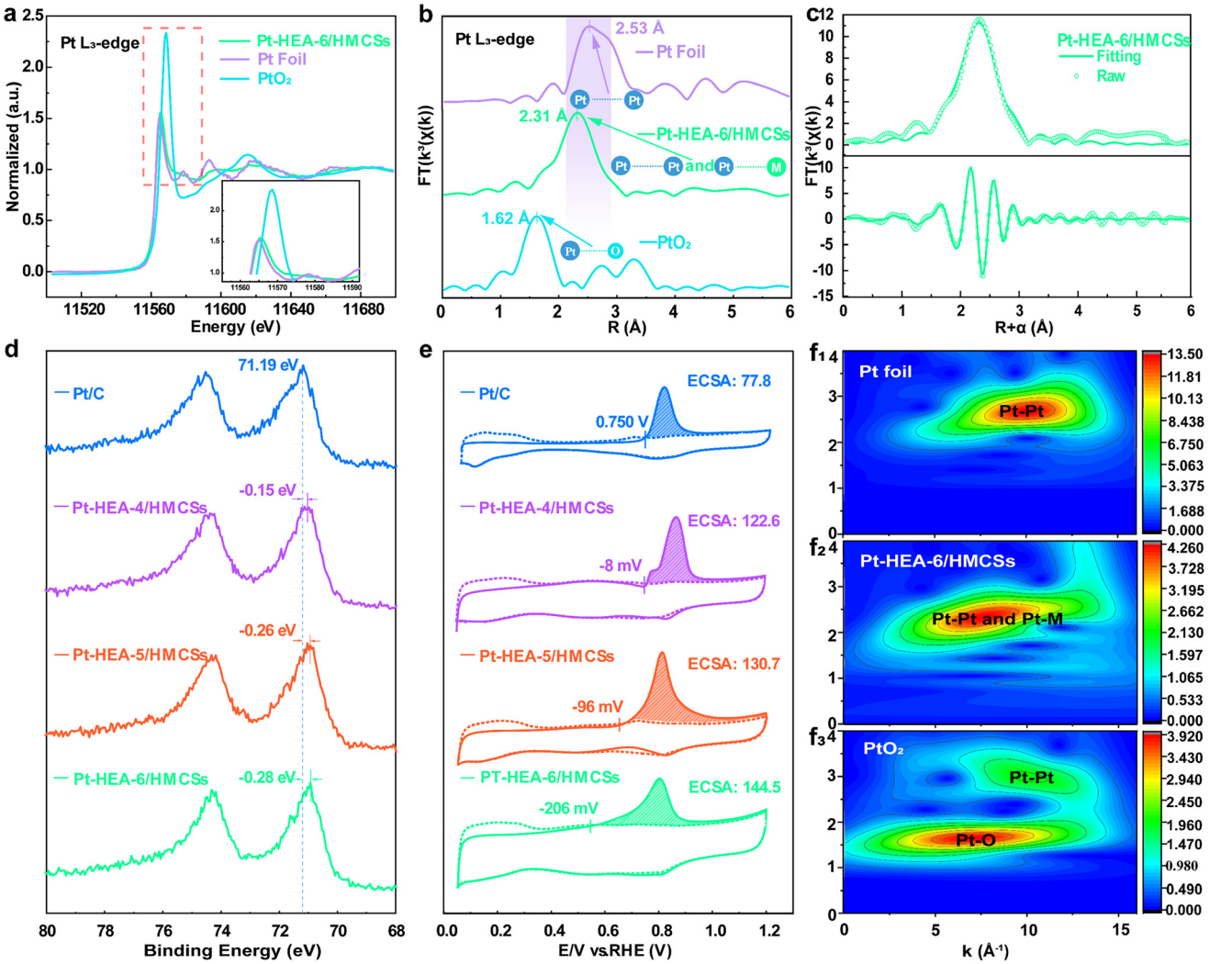

Fig. 3 (a) Pt L_3-edge XANES (inset is a regional enlargement view), (b) FT-EXAFS and wavelet transform plots for (f_1) Pt foil, (f_2) PtO_2, and (f_3) Pt-HEA-6/HMCSs; (c) fitting result of the *R*-space EXAFS spectrum for Pt-HEA-6/HMCSs; (d) XPS spectra of Pt/C and Pt-HEA-*x*/HMCSs; (e) voltammetry for electro-oxidation of adsorbed CO of the catalysts in 0.1 M $HClO_4$ at a scan rate of 30 mV s^{-1}.

samples, which collectively contribute to the enhanced electrocatalytic performance.[49]

X-ray photoelectron spectroscopy (XPS) analysis confirmed surface elemental makeup and valence states of the as-prepared samples (Fig. S8 and Table S3). The observed negative shift in Pt 4f binding energy relative to commercial Pt/C (Fig. 3d) indicates electron transfer from less electronegative transition metals to Pt, which reduces CO adsorption energy and enhances C–H bond activation, thereby improving electrocatalytic activity.[50] Deconvolution of the Pt 4f spectra revealed metallic and oxidized states (Fig. S9), while spectra of other transition metals are also presented (Fig. S10 and S11). In the Ru 3d XPS spectrum of Pt-HEA-6/HMCSs (Fig. S12), the peaks at 280.4, 281.1, and 281.3 eV can be deconvoluted into contributions from metallic Ru and ruthenium oxides. Elemental loadings quantified by XPS and EELS are summarized in Table S6, with results consistent with ICP analysis (Tables S4 and S5). Previous studies have linked the binding energy shift to improved anti-CO poisoning capability.[51] To verify this assumption, CO stripping experiments were carried out. The CO stripping voltammetry was performed in 0.1 M $HClO_4$ to evaluate the catalysts' anti-poisoning properties and electrochemical surface area (ECSA). As demonstrated in Fig. 3e, the CO oxidation onset potentials progressively decreased from 0.742 V for Pt-HEA-4/HMCSs to 0.654 V for Pt-HEA-5/HMCSs and further to a low of 0.544 V for Pt-HEA-6/HMCSs, representing negative shifts of 8, 96, and 206 mV relative to commercial Pt/C (0.750 V). This trend originates from the electronic modulation of Pt by the transition metals, consistent with XPS results. The onset potential for Pt/HMCSs (0.744 V) shifts negatively relative to the Pt/C benchmark (Fig. S13), owing to metal–support interactions that weaken *CO adsorption by engineering the electronic structure of Pt. Furthermore, the CO dissolution voltammogram of PtRu/C in Fig. S14 shows

© 2026 The Author(s). Co-published by the Institute of Process Engineering, Chinese Academy of Sciences and Royal Society of Chemistry

Open Access Article. Published on 31 March 2026. Downloaded on 5/11/2026 10:52:48 PM. This article is licensed under a Creative Commons Attribution-NonCommercial 3.0 Unported Licence.

that its onset potential is 706 mV, which is 44 mV lower than that of Pt/C. This indicates that the incorporation of Ru significantly amplifies the negative shift, as the oxophilic Ru promotes the generation of hydroxyl group (OH_{ads}) species, accelerating CO oxidation at lower potentials.[52] ECSA values derived from CO stripping (Table S7) increased with the HEA order degree: Pt-HEA-4/HMCSs (122.6 m^2 g_{Pt}^{-1}), Pt-HEA-5/HMCSs (130.7 m^2 g_{Pt}^{-1}), and Pt-HEA-6/HMCSs (144.5 m^2 g_{Pt}^{-1}), all exceeding Pt/C (77.8 m^2 g_{Pt}^{-1}). This indicates that the highly ordered Pt-HEA-6/HMCSs, with their optimal particle size, expose more active sites, thereby enhancing MOR activity.

To further understand the electronic structure of the sample, ultraviolet photoemission spectroscopy (UPS) is conducted to investigate the electronic properties of the catalysts. As shown in Fig. 4a–c, the work functions of the synthesized catalysts follow a decreasing trend: Pt-HEA-4/HMCSs (6.01 eV) > Pt-HEA-5/HMCSs (5.93 eV) > Pt-HEA-6/HMCSs (5.89 eV). This reduction, facilitated by Co or Ru doping, correlates with enhanced electron transfer efficiency and activated reaction thermodynamics.[53] The minimal work function of Pt-HEA-6/HMCSs signifies enhanced electrical conductivity. Additionally, the ionization potential offers insights into the catalyst's electron-donating propensity, where high electronegativity induces an electron-deficient environment. As indicated above, the incorporation of transition metals endows the HEA samples with a higher ionization potential relative to Pt/C (Fig. S15, E_i = 7.69 eV), which further optimizes the adsorption of oxygen-containing intermediates during the reaction process. Furthermore, Pt-HEA-6/HMCSs reach a maximum of approximately 2.32 eV, outperforming Pt-HEA-5/HMCSs (2.29 eV), Pt-HEA-4/HMCSs (2.22 eV), and Pt/C (1.66 eV), indicating a downshift of the valence state center in HEAs away from the Fermi level upon transition metal doping.[54] As shown in Fig. 4d, the shift of the valence state center away from the Fermi level manifests as a downward displacement of the HEA's d-band center. This weakens the adsorption of the toxic intermediate CO* and enhances the catalyst's anti-poisoning performance.[55]

2.2 The AOR activity of the HEA catalyst

The electrocatalytic performance of the as-prepared Pt-HEA/HMCS electrocatalysts for the methanol oxidation reaction (MOR) and ethanol oxidation reaction (EOR) was

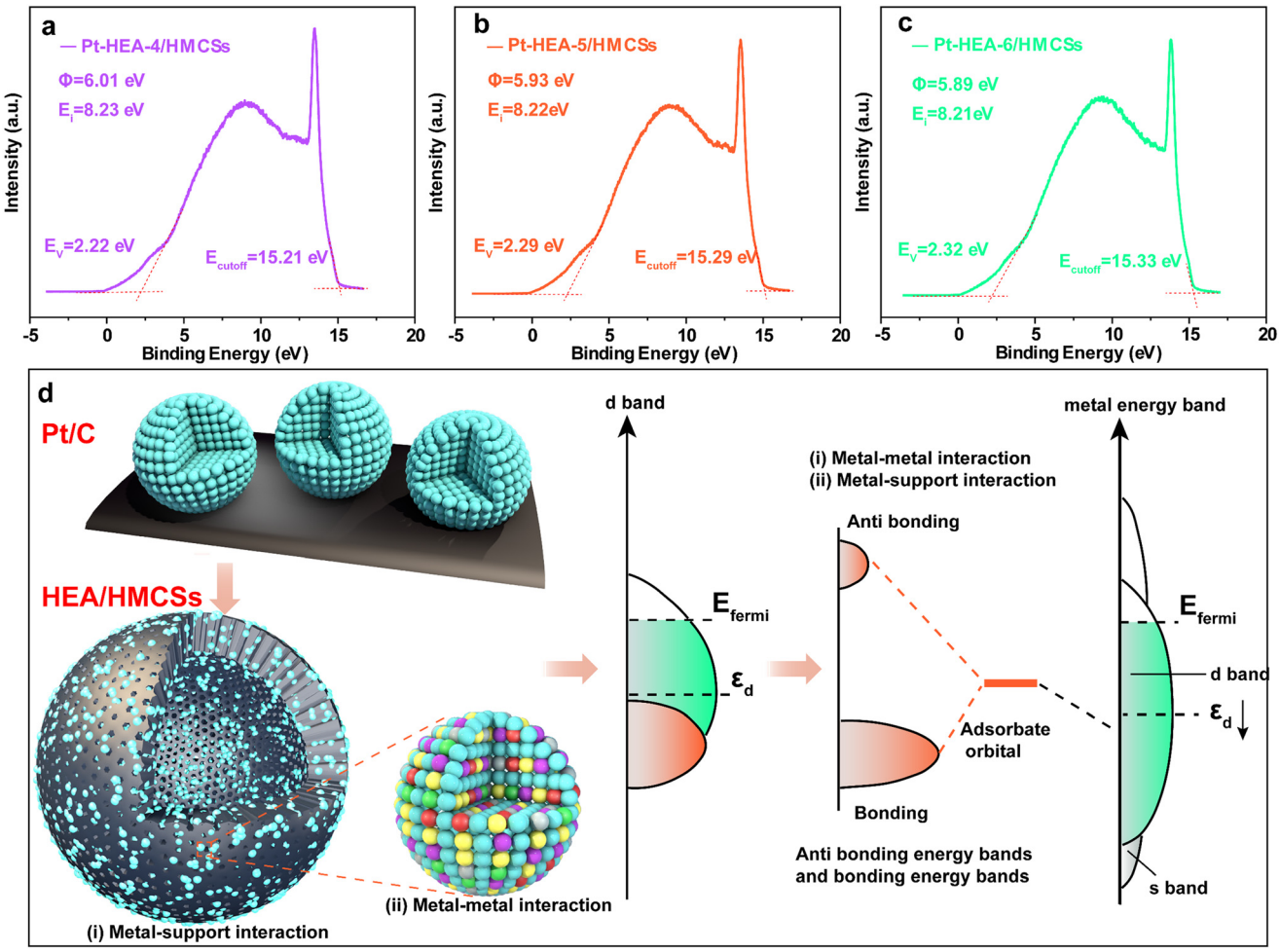

Fig. 4 UPS spectra of the synthesized catalysts: (a) Pt-HEA-4/HMCSs, (b) Pt-HEA-5/HMCSs, and (c) Pt-HEA-6/HMCSs; (d) schematic diagram of the downward shift of the HEA's d-band center.

© 2026 The Author(s). Co-published by the Institute of Process Engineering, Chinese Academy of Sciences and Royal Society of Chemistry

Open Access Article. Published on 31 March 2026. Downloaded on 5/11/2026 10:52:48 PM. This article is licensed under a Creative Commons Attribution-NonCommercial 3.0 Unported Licence.

systematically evaluated using cyclic voltammetry (CV). Initial electrochemical characterization in 0.1 M $HClO_4$ is provided in Fig. S16. Fig. 5a displays the MOR polarization curves; the Pt-HEA-6/HMCS catalyst exhibited a peak current density of 23.93 mA cm^{-2}, which is 3.17-fold, 1.67-fold, and 1.24-fold higher than those of Pt/C (7.55 mA cm^{-2}), Pt-HEA-4/HMCSs (14.34 mA cm^{-2}), and Pt-HEA-5/HMCSs (19.24 mA cm^{-2}). For reference, the current density achieved by Pt/HMCSs was also higher (9.58 mA cm^{-2}) than Pt/C (Fig. S17a). The shift in peak potential to slightly higher values reflect differences in surface kinetics and intermediate adsorption/desorption behavior. The MOR onset potential of Pt-HEA-6/HMCSs was measured at 0.33 V (Fig. 5b), demonstrating negative shifts of 110, 90, and 50 mV compared to those of Pt/C (0.44 V), Pt-HEA-4/HMCSs (0.42 V), and Pt-HEA-5/HMCSs (0.38 V). These findings confirm the enhanced electrocatalytic performance of the HEA nanoparticles, attributed to their site-specific atomic ordered arrangement, strong intermetallic interactions, and the large specific surface area of the porous carbon support. MA and SA, normalized by Pt loading and electrochemical surface area (ECSA), respectively, were further quantified. As shown in Fig. 5c, Pt-HEA-6/HMCSs achieved a MA of 1.54 mA μg_{Pt}^{-1} and a SA of 1.07 mA cm^{-2}, outperforming Pt-HEA-5/HMCSs (1.17 mA μg_{Pt}^{-1} and 0.90 mA cm^{-2}) and Pt-HEA-4/HMCSs (0.83 mA μg_{Pt}^{-1} and 0.68 mA cm^{-2}). Pt/HMCSs (MA: 0.41 mA μg_{Pt}^{-1} and SA: 0.49 mA cm^{-2}, Fig. S18a) also exceeded those of Pt/C (MA: 0.24 mA μg_{Pt}^{-1} and SA: 0.31 mA cm^{-2}). At a fixed potential of 1.0 V *vs.* RHE,

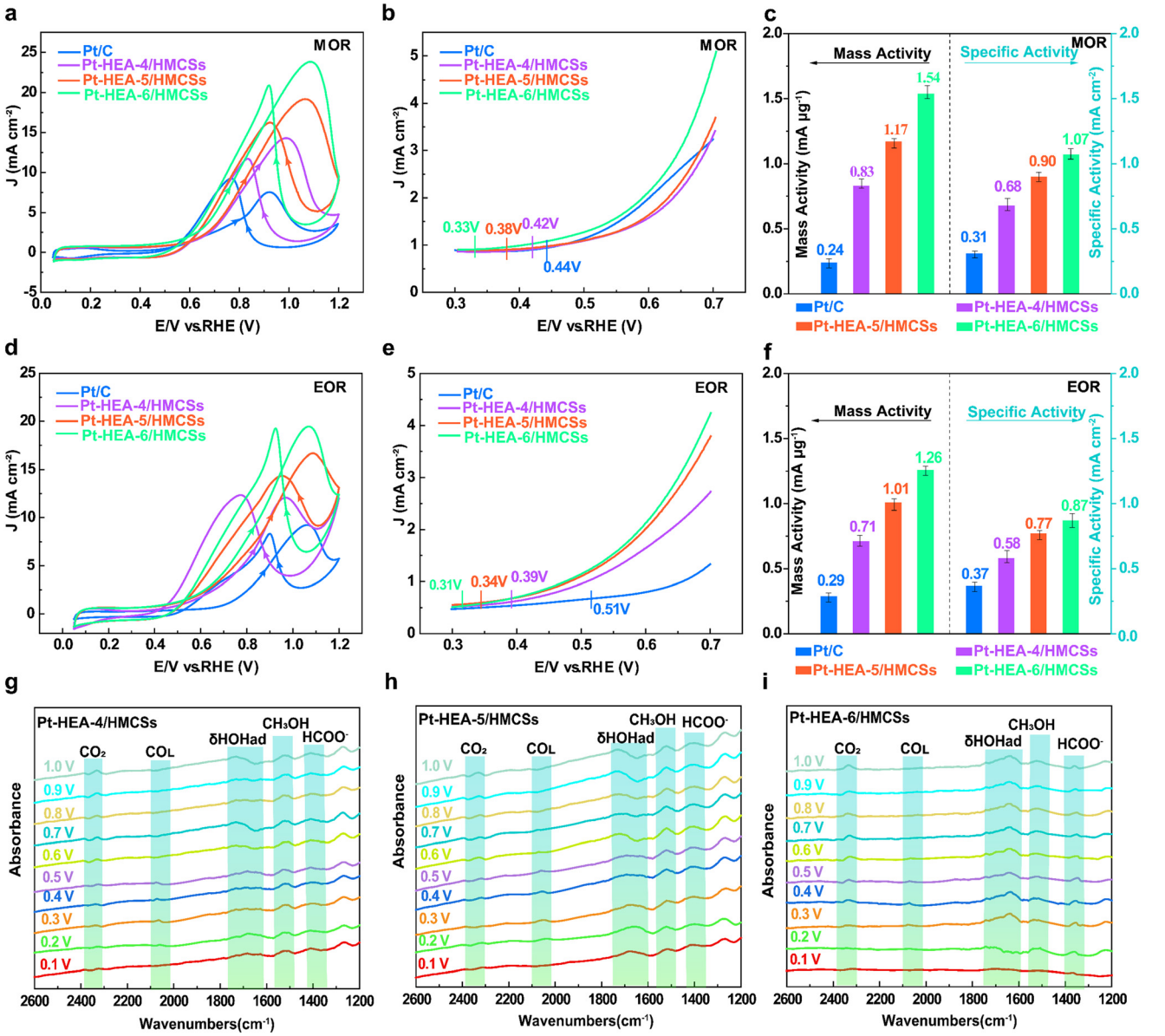

Fig. 5 Electrooxidation performance in 0.1 M $HClO_4$. (a) MOR CV curves at 50 mV s^{-1} in 0.5 M CH_3OH; (b) corresponding onset potentials; (c) MA and SA at the peak potential; (d) EOR CV curves in 0.5 M CH_3CH_2OH; (e) corresponding onset potentials; (f) MA and SA at the peak potential; *in situ* FTIR spectra during MOR on (g–i) Pt-HEA-*x*/HMCSs.

© 2026 The Author(s). Co-published by the Institute of Process Engineering, Chinese Academy of Sciences and Royal Society of Chemistry

Open Access Article. Published on 31 March 2026. Downloaded on 5/11/2026 10:52:48 PM. This article is licensed under a Creative Commons Attribution-NonCommercial 3.0 Unported Licence.

Pt-HEA-6/HMCSs exhibit the highest mass and specific activities among all catalysts (Fig. S19). A comprehensive comparison of MOR performance is summarized in Table S7. Fig. S20a shows that Pt-HEA-6/HMCSs have higher methanol oxidation activity than PtRu/C, confirming that the enhancement arises from entropy effects and strain engineering beyond Ru's bifunctional mechanism. EIS results (Fig. S20b) reveal its smallest charge transfer resistance, indicating the fastest reaction kinetics. To assess the general applicability of the catalysts for alcohol oxidation, ethanol oxidation reactions (EORs) were also conducted. In 0.5 M CH_3CH_2OH + 0.1 M $HClO_4$ (Fig. 5d), Pt-HEA-6/HMCSs delivered a peak current density of 19.55 mA cm^{-2}, which is 2.12, 1.60, and 1.18 times greater than those of Pt/C (9.23 mA cm^{-2}), Pt-HEA-5/HMCSs (16.63 mA cm^{-2}), and Pt-HEA-4/HMCSs (12.24 mA cm^{-2}). Pt/HMCSs (8.78 mA cm^{-2}) again surpassed Pt/C (Fig. S17b). The EOR onset potential for Pt-HEA-6/HMCSs was 0.31 V (Fig. 5e), lower than those of Pt-HEA-5/HMCSs (0.34 V), Pt-HEA-4/HMCSs (0.39 V), and Pt/C (0.51 V) by 30, 80, and 200 mV, respectively. The corresponding MA and SA for the EOR followed a similar trend (Fig. 5f), with Pt-HEA-6/HMCSs showing the highest values. Pt/HMCSs also exhibited improved MA and SA over the commercial Pt/C benchmark (Fig. S18b). A full comparison of EOR performance is provided in Table S8. To elucidate the potential-dependent pathways of methanol oxidation, *in situ* Fourier transform infrared-diffuse reflection (FTIR) measurements were carried out in an N_2-saturated solution of 0.1 M $HClO_4$ and 0.5 M CH_3OH. The spectra, collected between 0.1 and 1.0 V *vs.* RHE (Fig. 5g–i), revealed distinct absorption features in the 2600–1200 cm^{-1} region. The discernible ~1500 cm^{-1} band, assigned to the symmetric bending (scissoring) of adsorbed methyl species, was persistently discerned in the catalysts, corroborating the chemisorption of methanol.[56,57] Furthermore, reaction intermediates including $*CO_L$, δHOH_{ad}, and $COOH^-$ were identified. At potentials below 0.5 V, $*CO_L$ signals became observable on all catalysts. Upon increasing the potential, on Pt-HEA-6/HMCSs, the $*CO_L$ spectral signature disappeared almost simultaneously with the emergence of the CO_2 band at 0.5 V, indicating their efficient oxidation. In contrast, the $*CO_L$ features on Pt-HEA-5/HMCSs and Pt-HEA-4/HMCSs only began to diminish at 0.7 V, while the signal on Pt/C persisted even at 1.0 V (Fig. S21). This complete oxidation process liberated the Pt active sites, ensuring the persistence of methanol adsorption and oxidation. Such enhancement is primarily due to the tailored electronic structure, which weakens intermediate adsorption and collectively accelerates the reaction kinetics.[58] The improved performance, with Pt-HEA-6/HMCSs being the most active, originates from the synergistic effects of site-specific atomic ordering, an optimized electronic structure, and marked compressive lattice strain, further enhanced by the Ru-induced bifunctional mechanism.

Stability tests were performed for the HEA NP catalysts using chronoamperometry (2000 s). As shown in

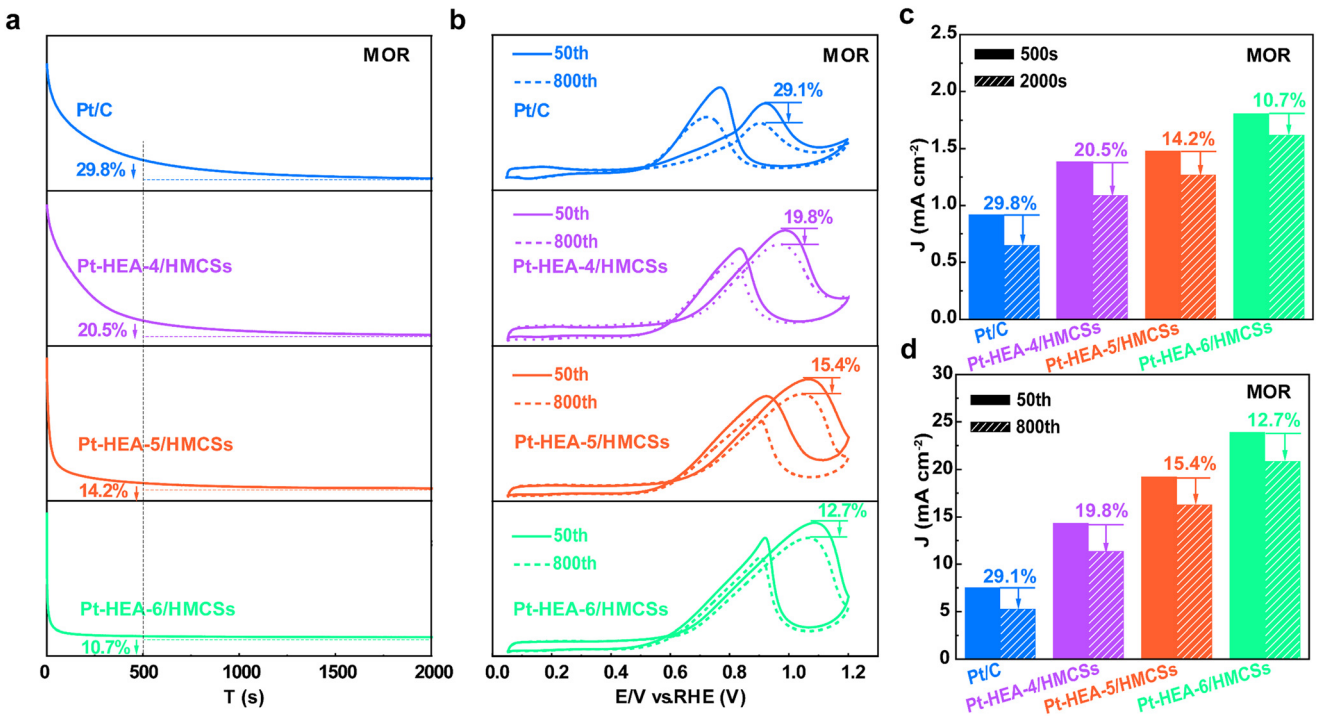

Fig. 6 (a) CA curves of the catalysts recorded at a constant potential in N_2-saturated 0.1 M $HClO_2$ + 0.5 M CH_3OH for 2000 s; (b) CV of the catalysts before and after 800-cycle accelerated durability tests at a scan rate of 50 mV s^{-1}; histograms comparing the current density decay rates after the (c) CA test and (d) 800-cycle durability test.

© 2026 The Author(s). Co-published by the Institute of Process Engineering, Chinese Academy of Sciences and Royal Society of Chemistry

Open Access Article. Published on 31 March 2026. Downloaded on 5/11/2026 10:52:48 PM. This article is licensed under a Creative Commons Attribution-NonCommercial 3.0 Unported Licence.

Fig. 6a and c, from 500 s to 2000 s, Pt/C, Pt-HEA-4/HMCSs, Pt-HEA-5/HMCSs, and Pt-HEA-6/HMCSs exhibited current density losses of 29.8%, 20.5%, 14.2%, and 10.7%, respectively. All catalysts exhibited a rapid current decay in the initial stage, which is commonly associated with the poisoning of active sites by adsorbed CO and other reaction intermediates.[59] Accelerated durability tests over 800 cycles in the same electrolyte further confirmed the superior stability of the HEA NPs (Fig. 6b and d). The current density losses after cycling were 12.7% for Pt-HEA-6/HMCSs, 15.4% for Pt-HEA-5/HMCSs, 19.8% for Pt-HEA-4/HMCSs, and 29.1% for Pt/C. Similar trends were observed in ethanol oxidation. CA tests (Fig. 7a and c) revealed current density declines of 11.8% (Pt-HEA-6/HMCSs), 16.7% (Pt-HEA-5/HMCSs), 19.9% (Pt-HEA-4/HMCSs), and 28.6% (Pt/C). After 800 accelerated durability test cycles (Fig. 7b and d), the corresponding losses were 11.2%, 18.2%, 20.0%, and 28.4%. For reference, Pt/HMCSs also exhibited better stability than Pt/C, with current density declines of 22.8% (CA) and 23.2% (accelerated durability tests) in methanol, and 25.2% (CA) and 24.7% (ADT) in ethanol (Fig. S22 and S23). Compared with PtRu/C, the 10 000 s CA test and the 800 cycles of accelerated durability tests both demonstrated that Pt-HEA-6/HMCSs exhibited better durability and stability (Fig. S24). Furthermore, 5000 cycles of accelerated durability CV tests also demonstrated that Pt-HEA-6/HMCSs have excellent durability (Fig. S25). The enhanced stability and durability of HEA NPs over Pt/C stem from a synergistic effect between the corrosion-resistant HMCS support and the anchored metal atoms. This is exemplified by Pt-HEA-6/HMCSs, which deliver the best performance due to a higher degree of site-specific atomic order, substantial lattice strain, and an optimized coordination environment.

3 Conclusions

In summary, we constructed Pt-HEA-*x*/HMCS electrocatalysts toward high-performance MOR, achieving nanoparticles (NPs) with precisely controlled compositions and site-specific ordering on HMCSs by employing a precision thermal field-guided silica confinement strategy that drives site-specific substitution into a chemically ordered phase. AC-HAADF-STEM imaging confirmed a site-specific atomic ordered structure exhibiting compressive lattice strain, evidenced by the interplanar spacings of d_{111} = 0.213 nm and d_{110} = 0.269 nm. XAFS data confirm the presence of contracted metal–metal bonds in Pt-HEA-6/HMCSs, showing a shortened Pt–M bond length (2.31 Å) compared to Pt foil (2.53 Å). The reduced Pt–Pt coordination number (11.24) indicates an optimized coordination environment and a modulated electronic structure, which collectively enhance CO tolerance and accelerate electrocatalytic kinetics. More importantly, the introduction of Co atoms leads to a significant enhancement in their structural ordering. Furthermore, the bifunctional mechanism introduced by the subsequent incorporation of Ru enhances the tolerance of the toxic intermediate, thereby promoting the electrocatalytic reaction kinetics. Specifically, the improved electrocatalytic performance of the Pt-HEA-6/

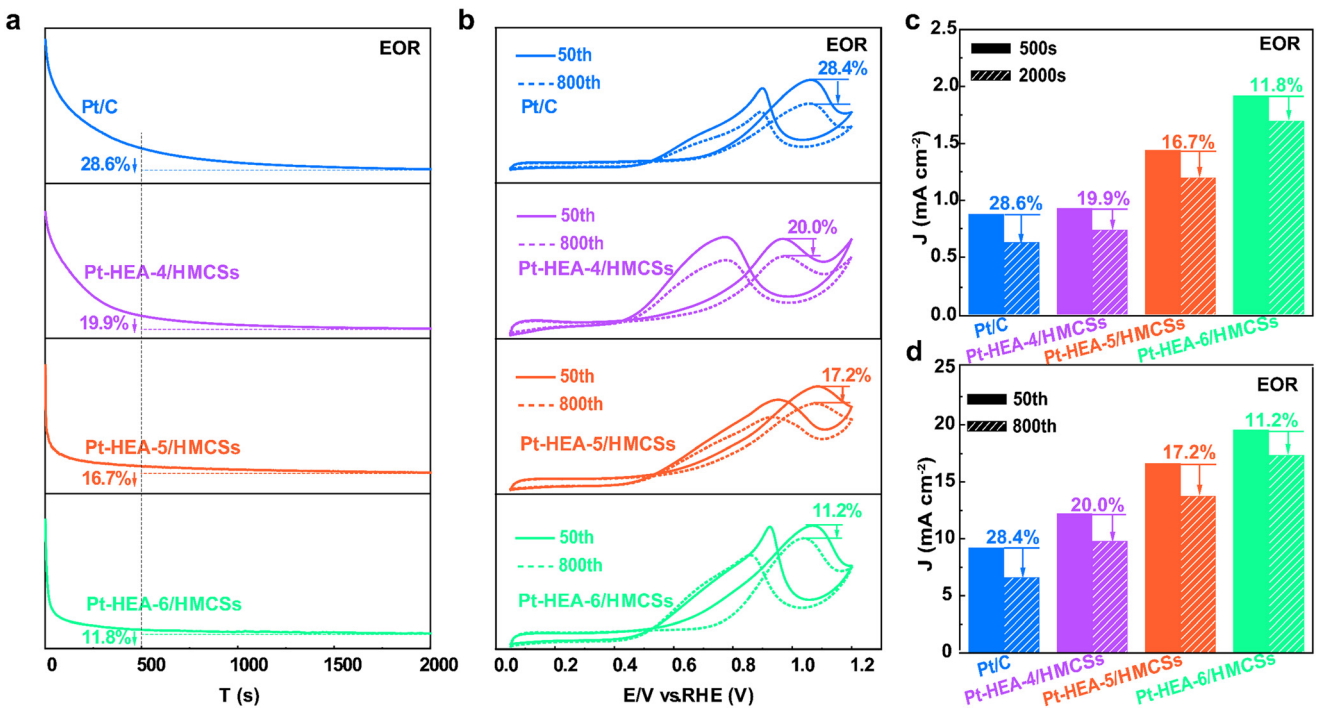

Fig. 7 (a) CA curves of the catalysts in N_2-saturated 0.1 M $HClO_4$ + 0.5 M CH_3CH_2OH for 2000 s; (b) CV of the catalysts before and after 800-cycle durability tests at a scan rate of 50 mV s^{-1}; histograms comparing the current density decay rates after the (c) CA test and (d) 800-cycle durability test.

© 2026 The Author(s). Co-published by the Institute of Process Engineering, Chinese Academy of Sciences and Royal Society of Chemistry

Open Access Article. Published on 31 March 2026. Downloaded on 5/11/2026 10:52:48 PM. This article is licensed under a Creative Commons Attribution-NonCommercial 3.0 Unported Licence.

HMCS electrocatalyst, attributed to its site-specific atomic ordering and optimized coordination environment, was manifested by a 6.42-fold increase in MA and a 3.45-fold increase in SA relative to Pt/C, paired with superior CO resistance evidenced by a −206 mV shift in onset potential. And the enhanced activity originates from the site-specific atomic ordering and optimized coordination environment, combined with the lattice compressive strain, as well as the structural advantages of the small particle diameter and high surface area of the HMCS support, which collectively expose abundant active sites, complemented by entropic stabilization and strong metal–support coupling. While the higher ECSA contributes to the enhanced apparent activity, the intrinsically higher catalytic efficiency per active site, demonstrated by the 3.45-fold higher specific activity, and the systematic increase in ordering degree from 0.33 to 0.43 across the HEA samples, together with the contracted Pt–M bond length (2.31 Å) and the 206 mV negative shift in CO oxidation onset potential, confirm that the performance improvement arises from synergistic contributions beyond surface area, including optimized electronic structure, lattice strain, and atomic ordering. The strategy presented herein enables the construction of site-specific atomic ordering HEA electrocatalysts that exhibit superior activity, extended stability, and CO resistance in the MOR and EOR. These improvements represent a key step toward viable DMFCs.

4 Experimental section

4.1 Materials

The synthesis utilized aqueous solutions of the following metal precursors: $H_2PtCl_6{\cdot}6H_2O$ (19.75 mg mL^{-1}), $Fe(NO_3)_3{\cdot}6H_2O$ (0.5 M), $NiCl_2$ (0.1 M), $CuSO_4$ (0.1 M), $Co(NO_3)_2{\cdot}6H_2O$ (0.5 M) and $RuCl_3$ (18.15 mg mL^{-1}), ammonium hydroxide ($NH_3{\cdot}H_2O$, AR, 25–28%), HCl (0.1 M), tetrapropyl orthosilicate ($(CH_3CH_2CH_2O)_4Si$, TPOS, 97 wt%), tetraethyl orthosilicate ($Si(OC_2H_5)_4$, TEOS, 98 wt%), resorcinol ($C_6H_6O_2$, AR, 99%), formaldehyde (CH_2O, 37–40 wt%), HF (30 wt%), and CH_3CH_2OH (AR, ≥95.5 wt%) were purchased from Macklin. Deionized (DI) water from the Milli-Q System (Millipore, Billerica, MA) was used in all our experiments. A 5 wt% Nafion solution was purchased from Aldrich. The commercial Pt/C catalyst (JM, 20 wt% Pt loading) was procured from Sunlaite. The 20 wt% Pt/C catalyst has ~3 nm Pt nanoparticles loaded on a Vulcan XC-72 carbon support. All the chemicals were used as purchased without any further purification.

4.2 Preparation of SiO_2@SiO_2/RF

To prepare the precursor solution, 70 mL of CH_3CH_2OH, 10 mL of ultrapure water, 3 mL of ammonium hydroxide, and 3.5 mL of TPOS were mixed under ultrasonic treatment for 15 minutes. Then, 0.4 g of resorcinol and 0.56 mL of formaldehyde were mixed with the as-prepared solution to obtain resorcinol–formaldehyde (RF) resin. After stirring at room temperature for 24 h, the SiO_2@SiO_2/RF nanospheres were collected by centrifugation with ethanol several times.

4.3 Preparation of PtFeNiCuCoRu/HMCSs

The precursors were chosen for their compatible reduction potentials to enable co-reduction and atomic-scale mixing. Annealing at 800 °C (2 °C min^{-1}, 120 min) overcomes mixing enthalpy barriers and achieves homogeneous alloying without excessive particle growth. Although rapid heating/cooling rates (>10^4 K s^{-1}) can suppress phase separation, our moderate rate within the silica-confined strategy maintains dispersion while ensuring complete reduction. The hollow mesoporous carbon spheres provide high surface area and spatial confinement to prevent agglomeration. This synthesis builds on previous thermal shock and silica-templating methods for HEAs and porous carbons.

250 mg of SiO_2@SiO_2/RF, 20 mL of CH_3CH_2OH, and 20 mL of ultrapure water were ultrasonically dispersed for 30 minutes. Metal precursors (865 μL $H_2PtCl_6{\cdot}6H_2O$, 200 μL each of $Fe(NO_3)_3$, $NiCl_2$, $CuSO_4$, $Co(NO_3)_2$, $RuCl_3$) were combined with the initial mixture and stirred at room temperature for 24 h. Subsequently, 3 mL of $Si(OCH_2CH_5)_4$ and 2 mL of HCl were added; after 30 minutes of stirring, the mixture was dried at 60 °C for 24 h. The product was then annealed under 5% H_2 and 95% N_2 (with a temperature program from 20 °C to 800 °C at 2 °C min^{-1}, followed by a 120-minute hold) to concurrently form PtFeNiCuCoRu; meanwhile the carbonization of silica@silica/resorcinol formaldehyde (SiO_2@SiO_2/RF) yields SiO_2@SiO_2/C. The silica template was etched by stirring in 30 wt% HF for 24 h to yield hollow mesoporous carbon spheres (HMCSs). The final Pt-HEA-6/HMCSs (PtFeNiCuCoRu/HMCSs) were collected *via* centrifugation, underwent five washing cycles with ethanol/water, and dried. Pt-HEA-4/HMCSs (PtFeNiCu/HMCSs), Pt-HEA-4/HMCSs (PtFeNiCuCo/HMCSs) and Pt/HMCSs were synthesized analogously by adjusting the precursor composition.

All potentials reported in this work are referenced to the reversible hydrogen electrode (RHE).

Data availability

Data will be made available on request.

Supplementary information (SI) is available. See DOI: https://doi.org/10.1039/d6im00028b.

Author contributions

Guangtao Mao: data curation, writing – original draft. Xiyue Han: data curation, formal analysis. Yuan Xiong: formal analysis. Leqing Luo: supervision. Zhouxun Zeng: formal analysis. Qingmei Wang: supervision, writing – review & editing.

© 2026 The Author(s). Co-published by the Institute of Process Engineering, Chinese Academy of Sciences and Royal Society of Chemistry

Open Access Article. Published on 31 March 2026. Downloaded on 5/11/2026 10:52:48 PM. This article is licensed under a Creative Commons Attribution-NonCommercial 3.0 Unported Licence.

Conflicts of interest

The authors declare that they have no known competing financial interests or personal relationships that could have appeared to influence the work reported in this paper.

Acknowledgements

This research work was financially supported by the National Natural Science Foundation of China (No. 22408067), the Key Project of Guizhou Province Basic Research Program (ZD-[2025]-077), and the Guizhou Science and Technology Platform Foundation (No. ZSYS [2025]-033), and supported by the Sichuan Science and Technology Program (2026YFHZ0118).

References

1 A. Kumar, P. Daw and D. Milstein, Homogeneous catalysis for sustainable energy: Hydrogen and methanol economies, fuels from biomass, and related topics, *Chem. Rev.*, 2022, **122**, 385–441.
2 K. Wan, T. Chu, B. Li, P. Ming and C. Zhang, Rational design of atomically dispersed metal site electrocatalysts for oxygen reduction reaction, *Adv. Sci.*, 2023, **10**, 2203391.
3 J. Guo, Y. Haghshenas, Y. Jiao, P. Kumar, B. I. Yakobson, A. Roy, Y. Jiao, K. Regenauer-Lieb, D. Nguyen and Z. Xia, Rational design of earth-abundant catalysts toward sustainability, *Adv. Mater.*, 2024, **36**, 2407102.
4 A. G. Olabi and M. A. Abdelkareem, Renewable energy and climate change, *Renewable Sustainable Energy Rev.*, 2022, **158**, 112111.
5 M. K. Debe, Electrocatalyst approaches and challenges for automotive fuel cells, *Nature*, 2012, **486**, 43–51.
6 B. C. Ong, S. K. Kamarudin and S. Basri, Direct liquid fuel cells: A review, *Int. J. Hydrogen Energy*, 2017, **42**, 10142–10157.
7 Y. Yu, Q. Wang, X. Li, Q. Xie, K. Xu, S. Zhang, H. Zhang, M. Gong and W. Lei, Laser-thermal reduction synthesis of high-entropy alloys towards high-performance pH universal hydrogen evolution reaction, *Nano Mater. Sci.*, 2025, **7**, 400–408.
8 I. Martinaiou, A. H. A. Monteverde Videla, N. Weidler, M. Kübler, W. D. Z. Wallace, S. Paul, S. Wagner, A. Shahraei, R. W. Stark, S. Specchia and U. I. Kramm, Activity and degradation study of an Fe-N-C catalyst for ORR in direct methanol fuel cell (DMFC), *Appl. Catal., B*, 2020, **262**, 118217.
9 J. Wang, B. Zhang, W. Guo, L. Wang, J. Chen, H. Pan and W. Sun, Toward electrocatalytic methanol oxidation reaction: Longstanding debates and emerging catalysts, *Adv. Mater.*, 2023, **35**, 2211099.
10 C. Ding, F. Dong and Z. Tang, Research progress on catalysts for the electrocatalytic oxidation of methanol, *ChemistrySelect*, 2020, **5**, 13318–13340.
11 P. Wang, R. Zhang, K. Wang, Y. Liu, L. Zhang, X. Wang, H. Li, Y. He and Z. Liu, Simultaneously constructing asymmetrically coordinated cobalt single atoms and cobalt nanoclusters via a fresh potassium hydroxide clipping strategy toward efficient alkaline oxygen reduction reaction, *Energy Mater. Adv.*, 2023, **4**, 42.
12 M. Mansor, S. N. Timmiati, K. L. Lim, W. Y. Wong, S. K. Kamarudin and N. H. N. Kamarudin, Recent progress of anode catalysts and their support materials for methanol electrooxidation reaction, *Int. J. Hydrogen Energy*, 2019, **44**, 14744–14769.
13 H. Tian, Y. Yu, Q. Wang, J. Li, P. Rao, R. Li, Y. Du, C. Jia, J. Luo, P. Deng, Y. Shen and X. Tian, Recent advances in two-dimensional Pt based electrocatalysts for methanol oxidation reaction, *Int. J. Hydrogen Energy*, 2021, **46**, 31202–31215.
14 Z. Wu, L. Feng, Z. Lu, X. Yu, Y. Zhao, J. Luo, S. Wang, X. Tian and Q. Chen, Covalent organic frameworks/carbon nanotubes composite with cobalt(II) pyrimidine sites for bifunctional oxygen electrocatalysis, *Nano Mater. Sci.*, 2024, **6**, 419–427.
15 H. Cheng, J. Wang, C. Wu and Z. Liu, Electrocatalysts for formic acid-powered PEM fuel cells: challenges and prospects, *Energy Mater. Adv.*, 2023, **4**, 0067.
16 X. L. Tian, L. Wang, P. Deng, Y. Chen and B. Y. Xia, Research advances in unsupported Pt-based catalysts for electrochemical methanol oxidation, *J. Energy Chem.*, 2017, **26**, 1067–1076.
17 Y. Tong, X. Yan, J. Liang and S. X. Dou, Metal-based electrocatalysts for methanol electro-oxidation: Progress, opportunities, and challenges, *Small*, 2021, **17**, 1904126.
18 X. Wang, S. Xi, W. S. V. Lee, P. Huang, P. Cui, L. Zhao, W. Hao, X. Zhao, Z. Wang, H. Wu, H. Wang, C. Diao, A. Borgna, Y. Du, Z. G. Yu, S. Pennycook and J. Xue, Materializing efficient methanol oxidation via electron delocalization in nickel hydroxide nanoribbon, *Nat. Commun.*, 2020, **11**, 4647.
19 D. Wu, W. Zhang and D. Cheng, Facile synthesis of Cu/NiCu electrocatalysts integrating alloy, core-shell, and one-dimensional structures for efficient methanol oxidation reaction, *ACS Appl. Mater. Interfaces*, 2017, **9**, 19843–19851.
20 X. Yue, C. He, C. Zhong, Y. Chen, S. P. Jiang and P. K. Shen, Fluorine-doped and partially oxidized tantalum carbides as nonprecious metal electrocatalysts for methanol oxidation reaction in acidic media, *Adv. Mater.*, 2016, **28**, 2163–2169.
21 O.-G. Dragos-Pinzaru, L. Racila, G. Buema, I. Tabakovic and N. Lupu, Improvement of the electrocatalytic properties for the methanol oxidation reaction (MOR) of the CoPt alloy, *Coatings*, 2024, **14**, 17.
22 A. S. Duke, K. Xie, J. R. Monnier and D. A. Chen, Superior long-term activity for a Pt-Re alloy compared to Pt in methanol oxidation reactions, *Surf. Sci.*, 2017, **657**, 35–43.
23 Z. Wang, S. Zhou, W. Liao, Q. Zhou, M. Chen, J. Long and Q. Wang, Revealing the effect of surface composition on multiwalled carbon nanotubes supported Pt-Fe alloy electrocatalysts for methanol oxidation performance, *Chem. – Eur. J.*, 2022, **28**, e202201987.
24 B. Talluri, K. Yoo and J. Kim, Ultra-small Cu-Ni nanoalloy as a high-performance supercapacitor electrode material and

© 2026 The Author(s). Co-published by the Institute of Process Engineering, Chinese Academy of Sciences and Royal Society of Chemistry

Open Access Article. Published on 31 March 2026. Downloaded on 5/11/2026 10:52:48 PM. This article is licensed under a Creative Commons Attribution-NonCommercial 3.0 Unported Licence.

highly durable methanol oxidation electrocatalyst, *J. Ind. Eng. Chem.*, 2021, **102**, 95–102.

25 A. Zhang, J. Zhang, J. Zheng and Z. Wang, Pt-Au alloy nanoparticles synthesized by glow discharge plasma for enhanced methanol oxidation reaction performance, *Plasma Processes Polym.*, 2024, **21**, 2200179.

26 J. Lan, C. Li, T. Liu and Q. Yuan, One-step synthesis of porous PtNiCu trimetallic nanoalloy with enhanced electrocatalytic performance toward methanol oxidation, *J. Saudi Chem. Soc.*, 2019, **23**, 43–51.

27 Q. Zhang, Y. Xie, X. Zhang, M. Zhao, Q. Chen, Y. Wu, J. Yu, Q. Pan, F. Yang and H. Lin, Construction of ternary PtRuPd alloy supported on carbon nanotubes for concentrated methanol oxidation, *ChemCatChem*, 2023, **15**, e202300255.

28 D. Zhang, L. Si, Q. Ren, X. Yan and S. Hu, Competitive intermetallics formation in Pd-Zn-Cd system via seeded growth from ultra-thin Pd nanosheets for electrocatalytic ethanol oxidation reaction, *Nano Res.*, 2024, **17**, 8552–8559.

29 Y. Li, Z. Yao, W. Gao, W. Shang, T. Deng and J. Wu, Nanoscale design for high entropy alloy electrocatalysts, *Small*, 2024, **20**, 2310006.

30 Y. Zhou, X. Shen, M. Wang, L. Zhang, T. Qian, C. Yan and J. Lu, The understanding, rational design, and application of high-entropy alloys as excellent electrocatalysts: A review, *Sci. China Mater.*, 2023, **66**, 2527–2544.

31 J. You, R. Yao, W. Ji, Y. Zhao and Z. Wang, Research of high entropy alloys as electrocatalyst for oxygen evolution reaction, *J. Alloys Compd.*, 2022, **908**, 164669.

32 X. Shan, Y. Pan, F. Cai, H. Gao, J. Xu, D. Liu, Q. Zhu, P. Li, Z. Jin, J. Jiang and M. Zhou, Accelerating the discovery of efficient high-entropy alloy electrocatalysts: high-throughput experimentation and data-driven strategies, *Nano Lett.*, 2024, **24**, 11632–11640.

33 N. Ullah, K. Aljohani, B. S. Aljohani, A. Ali, A. Ullah and S. Ullah, Ni/Co-based bouquet-like electrocatalyst for urea oxidation and supercapacitor applications, *Energy Technol.*, 2026, **14**, e202501672.

34 N. Ullah, S. Chmiel, D. Guziejewski, S. Khan, S. Hussain and M. Malecka, Copper selenide nanobelts an electrocatalyst for methanol electro-oxidation reaction, *Ionics*, 2023, **29**, 5363–5368.

35 S. Hua, S. A. Shah, N. Ullah, N. Ullah and A. Yuan, Synthesis of Fe_2O_3 nanorod and $NiFe_2O_4$ nanoparticle composites on expired cotton fiber cloth for enhanced hydrogen evolution reaction, *Molecules*, 2024, **29**, 3082.

36 L. Zhang, W. Cai, N. Bao and H. Yang, Implanting an electron donor to enlarge the d-p hybridization of high-entropy (oxy) hydroxide: A novel design to boost oxygen evolution, *Adv. Mater.*, 2022, **34**, 2110511.

37 D. Wang, Q. Li, C. Han, Q. Lu, Z. Xing and X. Yang, Atomic and electronic modulation of self-supported nickel-vanadium layered double hydroxide to accelerate water splitting kinetics, *Nat. Commun.*, 2019, **10**, 3899.

38 X. Cui, Y. Liu, X. Wang, X. Tian, Y. Wang, G. Zhang, T. Liu, J. Ding, W. Hu and Y. Chen, Rapid high-temperature liquid shock synthesis of high-entropy alloys for hydrogen evolution reaction, *ACS Nano*, 2024, **18**, 2948–2957.

39 X. Huang, Z. Wu, B. Zhang, G. Yang, H.-F. Wang, H. Wang, Y. Cao, F. Peng, S. Li and H. Yu, Formation of disordered high-entropy-alloy nanoparticles for highly efficient hydrogen electrocatalysis, *Small*, 2024, **20**, 2311631.

40 A. Ashok, A. Kumar, J. Ponraj, S. A. Mansour and F. Tarlochan, Enhancing the electrocatalytic properties of $LaMnO_3$ by tuning surface oxygen deficiency through salt assisted combustion synthesis, *Catal. Today*, 2021, **375**, 484–493.

41 H. Zhang, O. Nooan, X. Huang, Y. Yang, C. Xu, L. Zhou and C. Yu, Surfactant-Free assembly of mesoporous carbon hollow spheres with large tunable pore sizes, *ACS Nano*, 2016, **10**, 4579–4586.

42 Z. Li, J. Zhang, B. Y. Guan and X. W. Lou, Mesoporous carbon@titanium nitride hollow spheres as an efficient SeS_2 host for advanced Li-SeS_2 batteries, *Angew. Chem., Int. Ed.*, 2017, **56**, 16003–16007.

43 W. Huang, J. Chong, Y. Tian and X. Wang, Acid-programmed control of dual-mesoporous carbon nanospheres with predictable diameter, *Chem. Eng. J.*, 2017, **327**, 18–27.

44 D. Wang, Z. Chen, Y.-C. Huang, W. Li, J. Wang, Z. Lu, K. Gu, T. Wang, Y. Wu, C. Chen, Y. Zhang, X. Huang, L. Tao, C.-L. Dong, J. Chen, C. V. Singh and S. Wang, Tailoring lattice strain in ultra-fine high-entropy alloys for active and stable methanol oxidation, *Sci. China Mater.*, 2021, **64**, 2454–2466.

45 V. Tzitzios, X. Hu, K. Dimos, D. Gournis, V. Georgakilas, G. Avgouropoulos, M. S. Katsiotis, S. M. Alhassan and G. Hadjipanayis, Uniform growth of *fct* FePt nanoparticles on the surface of reduced-GO via a green facile approach. Ferromagnetic r-GO nanocomposites with high coercivity and surface area, *Carbon*, 2017, **121**, 209–216.

46 B. Zhang, C. Wang, D. Liu, Y. Liu, X. Yu and L. Wang, Boosting ORR electrocatalytic performance of metal-free mesoporous biomass carbon by synergism of huge specific surface area and ultrahigh pyridinic nitrogen doping, *ACS Sustainable Chem. Eng.*, 2018, **6**, 13807–13812.

47 T. Shen, D. Xiao, Z. Deng, S. Wang, L. An, M. Song, Q. Zhang, T. Zhao, M. Gong and D. Wang, Stabilizing diluted active sites of ultrasmall high-entropy intermetallics for efficient formic acid electrooxidation, *Angew. Chem., Int. Ed.*, 2024, **63**, e202403260.

48 P. Kuang, Y. Wang, B. Zhu, F. Xia, C.-W. Tung, J. Wu, H. M. Chen and J. Yu, Pt single atoms supported on N-doped mesoporous hollow carbon spheres with enhanced electrocatalytic H_2-evolution activity, *Adv. Mater.*, 2021, **33**, 2008599.

49 Z. Jia, T. Yang, L. Sun, Y. Zhao, W. Li, J. Luan, F. Lyu, L. C. Zhang, J. J. Kruzic, J. J. Kai, J. C. Huang, J. Lu and C. T. Liu, A novel multinary intermetallic as an active electrocatalyst for hydrogen evolution, *Adv. Mater.*, 2020, **32**, 2000385.

50 F. Yang, J. Ye, L. Gao, J. Yu, Z. Yang, Y. Lu, C. Ma, Y.-J. Zeng and H. Huang, Ultrathin PtNiGaSnMoRe senary nanowires with partial amorphous structure enable remarkable

© 2026 The Author(s). Co-published by the Institute of Process Engineering, Chinese Academy of Sciences and Royal Society of Chemistry

Open Access Article. Published on 31 March 2026. Downloaded on 5/11/2026 10:52:48 PM.
This article is licensed under a Creative Commons Attribution-NonCommercial 3.0 Unported Licence.

methanol oxidation electrocatalysis, *Adv. Energy Mater.*, 2023, **13**, 2301408.

51 L. Shen, B. Lu, X. Qu, J. Ye, J. Zhang, S. Yin, Q. Wu, R. Wang, S. Shen, T. Sheng, Y. Jiang and S. Sun, Does the oxophilic effect serve the same role for hydrogen evolution/oxidation reaction in alkaline media?, *Nano Energy*, 2019, **62**, 601–609.

52 Q. Wang, S. Chen, J. Jiang, J. Liu, J. Deng, X. Ping and Z. Wei, Manipulating the surface composition of Pt-Ru bimetallic nanoparticles to control the methanol oxidation reaction pathway, *Chem. Commun.*, 2020, **56**, 2419–2422.

53 J. Cheng, C. Lyu, H. Li, J. Wu, Y. Hu, B. Han, K. Wu, M. Hojamberdiev and D. Geng, Steering the oxygen reduction reaction pathways of N-carbon hollow spheres by heteroatom doping, *Appl. Catal., B*, 2023, **327**, 122470.

54 Z. Chen, Y. Song, J. Cai, X. Zheng, D. Han, Y. Wu, Y. Zang, S. Niu, Y. Liu, J. Zhu, X. Liu and G. Wang, Tailoring the d-band centers enables Co_4N nanosheets to be highly active for hydrogen evolution catalysis, *Angew. Chem., Int. Ed.*, 2018, **57**, 5076–5080.

55 X. Qi, N. Ye, R. Zhang, Z. Jiang and T. Fang, Boosting the activity and CO tolerance for methanol oxidation reaction in alkaline media by constructing the Pt-TMNs electrocatalysts, *Fuel*, 2023, **350**, 128773.

56 J. Zhang, X. Qu, Y. Han, L. Shen, S. Yin, G. Li, Y. Jiang and S. Sun, Engineering PtRu bimetallic nanoparticles with adjustable alloying degree for methanol electrooxidation: Enhanced catalytic performance, *Appl. Catal., B*, 2020, **263**, 118345.

57 W. Chen, S. Luo, M. Sun, X. Wu, Y. Zhou, Y. Liao, M. Tang, X. Fan, B. Huang and Z. Quan, High-entropy intermetallic PtRhBiSnSb nanoplates for highly efficient alcohol oxidation electrocatalysis, *Adv. Mater.*, 2022, **34**, 2206276.

58 Q. Wang, S. Chen, P. Li, S. Ibraheem, J. Li, J. Deng and Z. Wei, Surface Ru enriched structurally ordered intermetallic PtFe@PtRuFe core-shell nanostructure boosts methanol oxidation reaction catalysis, *Appl. Catal., B*, 2019, **252**, 120–127.

59 T. He, W. Wang, F. Shi, X. Yang, X. Li, J. Wu, Y. Yin and M. Jin, Mastering the surface strain of platinum catalysts for efficient electrocatalysis, *Nature*, 2021, **598**, 76–81.

© 2026 The Author(s). Co-published by the Institute of Process Engineering, Chinese Academy of Sciences and Royal Society of Chemistry